Cement and Concrete Research 129 (2020) 105890

Contents lists available at ScienceDirect

Cement and Concrete Research

journal homepage: www.elsevier.com/locate/cemconres

High-dynamic compressive and tensile strength of specimens made of cementitious materials

E. Binder[a,b], R. Reihsner[b], Y. Yuan[a], H.A. Mang[a,b], B.L.A. Pichler[b,*]

[a] College of Civil Engineering, Tongji University, 1239 Siping Road, Shanghai, China
[b] Institute for Mechanics of Materials and Structures, TU Wien-Vienna University of Technology, Karlsplatz 13/202, 1040 Vienna, Austria

ARTICLE INFO

Keywords:
High-dynamic strength increase
Cement paste
Mortar
Concrete

ABSTRACT

The strength of specimens made of cementitious materials increases with increasing loading rate. Herein, the model of Fischer et al. (CCR 58, 2014, 186–200) is revisited in the context of high-dynamic compression and extended to high-dynamic tension. The model is based on the assumptions (i) that cracking will start if the quasi-static *material* strength is reached, and (ii) that the high-dynamic strength gain refers to the increase of the stress *during* the failure process of the tested specimen. The model explains the behavior of cylindrical specimens made of dry cement paste, mortar, and concrete, subjected to high-dynamic compression. It also elucidates the performance of cylindrical specimens made of dry mortar and concrete, subjected to high-dynamic tension. It is concluded that the high-dynamic strength gain is a structural effect and that structures will be damaged if the dynamic stress exceeds the quasi-static strength, no matter how fast the stress is increased and how short the stress pulse lasts.

1. Introduction

The strength of specimens made of cementitious materials increases with increasing loading rate, i.e., either with the strain rate or with the stress rate. This increase is significant in the high-dynamic regime, where the strain rates are larger than 10/s [1]. The high-dynamic strength gain is quantified by means of the Dynamic Strength Increase Factor (DIF), defined as

$$\mathrm{DIF} = \frac{f_{dyn}}{f_{sta}}, \tag{1}$$

where f_{dyn} denotes the dynamic strength and f_{sta} stands for the quasi-static strength. Notably, f_{sta} is standardly determined using a strain rate $\dot{\varepsilon} = 2 \times 10^{-5}$/s [2].

High-dynamic strain rates can be produced by drop-weight machines [3, 4] as well as by Split Hopkinson Pressure Bars (SHPBs). The latter were used to test specimens made of cement pastes [5], mortars [6-8], and concretes [9-15]. The data of the experiments, which are analyzed in the present paper, are summarized in Table 1. They refer to cylindrical specimens made of dry cementitious materials. Their diameters are denoted as d and their axial lengths as h.

Many analytical expressions for the DIF in both compression and tension can be found in the open literature, see, e.g., [16] for a selected collection of formulae, published within 1990–2015. They were either obtained by means of empirical fitting of experimental data or as results of modeling. As for the high-dynamic regime, the DIF was e.g. expressed by the authors of the *fib* Model Code [17] as a power-law function of the strain rate $\dot{\varepsilon}$. Expressions for the DIF as linear, quadratic, or cubic polynomials in $\log \dot{\varepsilon}$ were suggested e.g. in [6, 18-21]. A rational polynomial in $\dot{\varepsilon}$ was proposed e.g. in [22]. Fischer et al. [5] expressed the DIF in high-dynamic compression as a linear function of $\dot{\varepsilon}$. The present paper represents a continuation of this line of research.

As for modeling the high-dynamic strength gain in *compression*, rate-dependent material properties and inertial confinement are frequently accounted for. Rate-dependent material models are based on the assumption that the mechanical properties of cementitious materials are functions of the loading rate, such that e.g. strength-like quantities increase with increasing speed of loading. Approaches accounting for inertial confinement consider that, because of inertia forces, high-dynamic uniaxial loading results in triaxial *compressive* stress states. The latter result in an increase of the strength of a dynamically loaded specimen relative to the quasi-static uniaxial compressive strength of the material. Available models can be categorized as follows:

- Both inertial confinement *and* rate-dependent material behavior are

* Corresponding author.
E-mail addresses: eva.binder@tuwien.ac.at (E. Binder), roland.reihsner@tuwien.ac.at (R. Reihsner), yuany@tongji.edu.cn (Y. Yuan), herbert.mang@tuwien.ac.at (H.A. Mang), bernhard.pichler@tuwien.ac.at (B.L.A. Pichler).

https://doi.org/10.1016/j.cemconres.2019.105890
Received 7 February 2019; Received in revised form 19 August 2019; Accepted 27 August 2019
0008-8846/ © 2019 The Authors. Published by Elsevier Ltd. This is an open access article under the CC BY-NC-ND license (http://creativecommons.org/licenses/BY-NC-ND/4.0/).

Table 1
Experimental data from high-dynamic strength testing, taken from the literature.

Compression tests of cement paste specimens by Fischer et al. [5] h = 6.63 mm, d = 10.1 mm, f_{sta} = 48.2 MPa, E = 14.2 GPa, ν = 0.29, ρ = 1593 kg/m^3								
f_{dyn} [MPa]	74.15	42.01	74.41	48.6	65.4	114.26	132.73	164.39
$\dot{\varepsilon}$ [1/s]	700	200	500	500	500	500	1900	2100
f_{dyn} [MPa]	156.36	133.73	152.64	143.78				
$\dot{\varepsilon}$ [1/s]	2100	2100	2100	1900				
Compression tests of mortar specimens by Zhang et al. [12] h = 18.0 mm, d = 37.0 mm, f_{sta} = 51.0 MPa, E = 23.1 GPa, ν = 0.19, ρ = 2116 kg/m^3								
f_{dyn} [MPa]	70.66	73.82	74.75	75.11	75.61	79.67	81.66	86.57
$\dot{\varepsilon}$ [1/s]	49.46	71.01	85.09	130.74	153.16	183.52	219.90	205.48
f_{dyn} [MPa]	90.43	96.52	98.16	99.45	101.67	109.04		
$\dot{\varepsilon}$ [1/s]	295.02	337.87	345.60	322.94	330.32	453.30		
h = 25.0 mm, d = 50.0 mm, f_{sta} = 51.0 MPa, E = 23.1 GPa, ν = 0.19, ρ = 2116 kg/m^3								
f_{dyn} [MPa]	64.45	71.22	71.47	75.02	72.13	76.01	77.00	79.14
$\dot{\varepsilon}$ [1/s]	37.01	69.67	76.68	56.43	89.38	126.20	152.86	126.20
f_{dyn} [MPa]	82.03	88.80	93.34	93.75	98.62			
$\dot{\varepsilon}$ [1/s]	165.04	192.39	165.04	228.61	261.43			
Compression tests of concrete specimens by Kühn et al. [15] h = 80.0 mm, d = 50.0 mm, f_{sta} = 25.1 MPa, E = 32.0 GPa, ν = 0.20, ρ = 2400 kg/m^3								
f_{dyn} [MPa]	95.1	104.2	119.2	125.7	142.5			
$\dot{\varepsilon}$ [1/s]	136.6	150.1	185.5	190.0	202.7			
Tension tests of mortar specimens by Brara and Klepaczko [7, 8] h = 120 mm, d = 40.0 mm, f_{sta} = 5.0 MPa, E = 31.0 GPa, ν = 0.21, ρ = 2200 kg/m^3								
f_{dyn} [MPa]	22.5	25.0	25.5	27.5	28.0	29.5	30.0	31.0
$\dot{\varepsilon}$ [1/s]	40	42	19	30	35	22	32	45
f_{dyn} [MPa]	31.5	33.0	33.5	35.0	36.0	43.0	46.5	25.0
$\dot{\varepsilon}$ [1/s]	40	41	48	70	95	70	90	35.6
f_{dyn} [MPa]	29.7	35.0						
$\dot{\varepsilon}$ [1/s]	51.5	68.4						
Tension tests of concrete specimens by Erzar and Forquin [13, 14] h = 140 mm, d = 45.0 mm, f_{sta} = 3.6 MPa, E = 32.0 GPa, ν = 0.16, ρ = 2278 kg/m^3								
f_{dyn} [MPa]	7.7	8.8	7.8	9.5	11.1	10.6	11.2	10.8
$\dot{\varepsilon}$ [1/s]	33	43	50	72	70	80	89	110
f_{dyn} [MPa]	13.7	12.7						
$\dot{\varepsilon}$ [1/s]	130	130						

accounted for e.g. in [16, 20].

- Inertial confinement, combined with a rate-*in*dependent material law, is used e.g. in [10, 19, 22-25].
- Rate-dependent material models, free of inertial confinement, are used e.g. in [26-29].
- Rate-*in*dependent linear elasticity, free of inertial confinement, is used e.g. in [5, 30].

As for the high-dynamic strength gain in *tension*, the available models can be categorized in two groups. The first group refers to models accounting for inertia effects, see e.g. [16, 31, 32]. Inertia results in triaxial *tensile* stress states and, hence, in high-dynamic strength loss [33]. The latter must be overcompensated by rate-dependent material properties in order to reproduce the experimentally observed high-dynamic strength gain [33]. The second group of models is free of inertia effects and accounts for rate-independent material properties, see e.g. [34, 35].

In the present paper, the rate-*in*dependent model by Fischer et al. [5], which is free of inertia effects, is revisited in the context of the high-dynamic strength gain under compressive loading, with the aim to check the predictive capabilities of the model. Subsequently, it is investigated whether or not *the same* modeling concept can also explain high-dynamic uniaxial *tension* experiments. The elasto-brittle modeling approach is based on the hypotheses that

1. also under high-dynamic loading, cracking will start if the quasi-static strength of the material is reached,
2. cracks propagate at a speed which is approximately equal to the velocity of shear waves, and
3. the high-dynamic strength gain occurs during the failure process that lasts from the start of crack propagation to disintegration of the specimen.

In order to assess the performance of this approach, modeling results are compared with experimental data from five different testing campaigns, carried out in five different laboratories. As for high-dynamic compression, the analysis includes tests of cement paste specimens by Fischer et al. [5], mortar specimens by Zhang et al. [12], and concrete

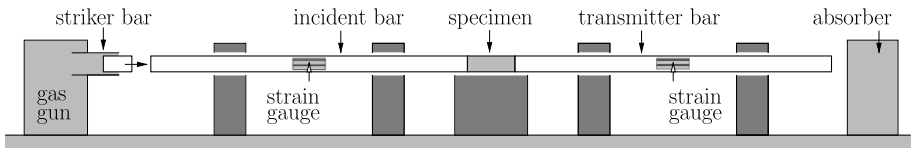

Fig. 1. Experimental setup of a Split Hopkinson Pressure Bar for a high-dynamic compression test.

specimens by Kühn et al. [15]. As for high-dynamic tension, the analysis includes tests of mortar specimens by Brara and Klepaczko [7, 8] as well as of concrete specimens by Erzar and Forquin [13, 14].

The present paper is structured as follows. In Section 2 the model of Fischer et al. [5] is revisited in the context of high-dynamic compression. Section 3 refers to the analysis of the aforementioned two series of high-dynamic tension experiments. Section 4 is devoted to the discussion of the obtained results. Section 5 contains the conclusions drawn from the present study.

2. Analysis of high-dynamic compression tests

SHPBs were used for high-dynamic compression tests analyzed in the present paper. The experimental setup consisted of a serial arrangement of a striker bar, an incident bar, a cylindrical specimen, a transmitter bar, and an adsorber, see Fig. 1. The striker bar was shot against the incident bar. The impact created a compression pulse, propagating along the incident bar. The pulse was partly transmitted and partly reflected at the interface between the incidental bar and the specimen. The transmitted compression pulse traveled along the specimen. It was partly transmitted and partly reflected at the interface between the specimen and the transmitter bar. The stress and strain histories experienced by the specimen can be computed by means of readings of strain gauges mounted to the incident and the transmitter bar [36]. This allowed for quantitative determination of the high-dynamic compressive strength of the specimen.

2.1. The elasto-brittle DIF-model by Fischer et al. (2014)

Fischer et al. [5] assumed that cracking will start if the quasi-static strength of the tested material is reached, and that a high-dynamic strength gain of the tested specimen occurs *during* the process of its failure. Denoting the duration of this process as $\Delta t_{failure}$ and the stress rate as $\dot{\sigma}$, the following analytical expression for f_{dyn} was obtained:

$$f_{dyn} = f_{sta} + \dot{\sigma}\ \Delta t_{failure}\ . \tag{2}$$

Setting $\Delta t_{failure}$ in Eq. (2) equal to the crack propagation length, ℓ, divided by the speed of the crack propagation, v_s, and inserting the resulting expression into Eq. (1) yields the following analytical expression for the DIF [5]:

$$\mathrm{DIF} = 1 + \frac{\dot{\sigma}}{f_{sta}}\,\frac{\ell}{v_s}. \tag{3}$$

The two quantities v_s and ℓ are discussed in the following two paragraphs.

According to classical fracture mechanics of brittle materials, the crack propagation velocity is limited by the Rayleigh wave speed [37]. Also atomic simulations of mode-I cracking along weak crystal interfaces have shown that the speed of propagation increases rapidly to the Rayleigh wave speed, to which it is limited, see Fig. 1 of [38]. This approach was adopted by Fischer et al. to micro-heterogeneous cementitious materials, containing a very large number of micro- and nanoscopic interfaces between the different constituents of their microstructures. Accordingly, it was assumed that cracks propagate at the shear wave speed, which serves as an estimate of the Rayleigh wave speed. The shear wave speed of an isotropic material is a function of Young's modulus E, Poisson's ratio ν, and the mass density ρ:

$$v_s = \sqrt{\frac{E}{2\,(1+\nu)\,\rho}}\,. \tag{4}$$

Notably, there are experimental studies where cracking at the Rayleigh wave speed was observed, see, e.g. [39]. Several other experimentalists, in turn, have reported that cracks propagated much less rapidly [40]. These measurements were based either on high-frequency photography or on electric wires attached to the surface of the tested specimens. It remains an open question whether or not such *surface-related* observations are representative for the crack propagation velocities *inside* the bulk of the tested specimens.

As regards ℓ, the approach of Fischer et al. suggests that the DIF is uncertain, because neither the position of the crack nucleation nor the direction of the crack propagation can be predicted. Still, Fischer et al. assumed that one value of ℓ could be used to re-analyze tests on nominally identical specimens, using the same testing machine for different high-dynamic loading rates. Treating ℓ as an optimization variable, its value is identified such as to achieve the best-possible agreement between DIF values obtained by Eq. (3) and experimental DIF data obtained from specific testing series. The plausibility of the identified value of ℓ can be assessed by comparing it with the upper bound, denoted as ℓ_{ub}. This bound refers to the special case where the crack nucleates at the outer contour of one of the circular surfaces of the cylindrical specimen and propagates diagonally through the specimen (Fig. 2), such that ℓ_{ub} follows as

$$\ell_{ub} = \sqrt{h^2 + d^2}\,. \tag{5}$$

The analysis of tests, for which the strain rate $\dot{\varepsilon}$ is reported by the experimentalists instead of $\dot{\sigma}$, requires a link between the two types of loading variables. Under the assumption of linear-elastic material behavior, this link is established by means of Hooke's law as

$$\dot{\sigma} = E\ \dot{\varepsilon}. \tag{6}$$

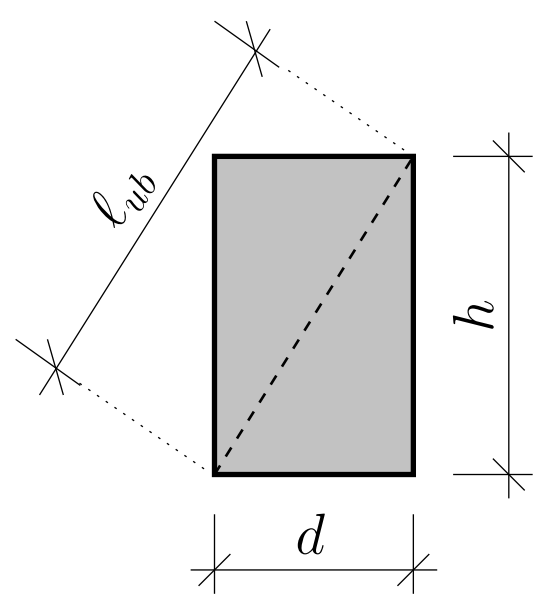

Fig. 2. Upper bound of the crack propagation length, ℓ_{ub}, according to Eq. (5), referring to a crack that nucleates at the outer contour of one of the circular surfaces of the cylindrical specimen and propagates diagonally through the specimen.

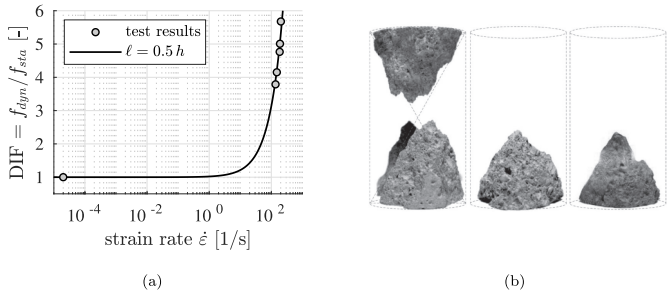

Fig. 3. High-dynamic compression tests of Kühn et al. [15] of concrete cylinders: (a) measured DIF values as a function of $\dot{\varepsilon}$ and modeling results according to Eqs. (3)–(7) with input values listed in Table 1, (b) photos showing fragments of specimens after testing.

2.2. Exemplary application of the DIF-model by Fischer et al. (2014)

Kühn et al. [15] subjected concrete cylinders to high-dynamic compression, see Table 1. An analytic expression for the DIF as a function of $\dot{\varepsilon}$ is obtained by inserting Eqs. (4)–(6) into Eq. (3). Evaluating the resulting expression for geometric and mechanical properties of the tested specimens, see Table 1, and optimizing the value of ℓ in order to minimize the square-root-of-sum-of-squared (SRSS) differences between measured and modeled DIF-values, yields

$$\ell = 0.49\,h, \tag{7}$$

see also Fig. 3 (a). The modeling results agree well with the experimental data, see Fig. 3 (a) and [41]. The optimal value of $\ell = 39.2$ mm, see Eq. (7), is smaller than the upper bound $\ell_{ub} = 94.3$ mm, see Eq. (5). In addition, it is interesting that photos of the fragments of the specimens after testing show residual cones, see Fig. 3. The characteristic crack length, measured from the "tip" of each cone to its base circle, is virtually equal to the identified value of ℓ, see Fig. 3.

Fischer et al. [5] subjected cement paste cylinders to high-dynamic compression. The remaining fragments of the specimens suggested crack propagation in the axial direction. This allows for the introduction of an improved upper bound and of a lower bound for ℓ:

1. If cracking started right at the interface between the cylindrical specimen and one of the load plates, the propagating crack edge would have to travel along the total axial length of the specimen. Thus, the improved upper bound reads as: $\ell_{ub} = h$.
2. If cracking started at the center of the specimen, two crack edges would propagate simultaneously. Each of them would have to cover a distance equal to one half of the axial length of the specimen. Thus, the lower bound reads as: $\ell_{\ell b} = h/2$.

Realistic scenarios must fall inside the following interval:

$$0.50\,h \le \ell \le 1.00\,h. \tag{8}$$

In order to reproduce measured DIF-values, Fischer et al. [5] treated ℓ as a fitting parameter. All other input values, required for quantification of the DIF according to Eqs. (3)–(6), are known, see Table 1. The minimum SRSS differences between measured and modeled DIF-values was obtained for

$$\ell = 0.59\,h, \tag{9}$$

see also Fig. 4. The optimum value of ℓ satisfies the two discussed bounds, see Eq. (8). This is seen as a further corroboration of the model.

The model suggests that the DIF increases linearly with the size of the specimen, because it is a linear function of ℓ, see Eq. (3), which is proportional to the axial length h of the specimen, see Eqs. (7) and (9). This provides the motivation to analyze experiments carried out with geometrically *similar* specimens of two *different* sizes. Such tests were performed by Zhang et al. [12], who subjected mortar cylinders to high-dynamic compression. The scaling ratio of the two tested sizes of specimens amounted to 18:25, see Table 1. In order to reproduce measured DIF-values obtained with the *smaller* specimens, ℓ is treated as a fitting parameter. All other input values required for quantification of the DIF according to Eqs. (3)–(6) are known, see Table 1. The minimum SRSS differences between measured and modeled DIF-values was obtained for

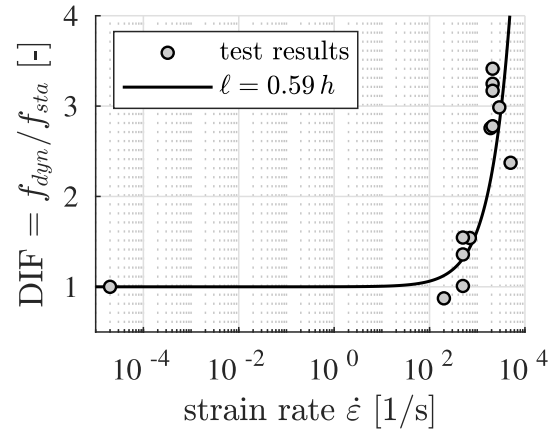

Fig. 4. High-dynamic compression tests of Fischer et al. [5] of cement paste cylinders: measured DIF values as a function of $\dot{\varepsilon}$ and modeling results according to Eqs. (3)–(6) and (9), with input values listed in Table 1.

$$\ell = 0.74\,h, \tag{10}$$

see also Fig. 5 (a). Because the tested specimens were geometrically similar, the relation between ℓ and h, found for the smaller specimens, see Eq. (10), *must* also apply to the larger ones. This is checked by *predicting* DIF-values for the larger specimens by means of the Eqs. (3)–(6) and (10) and the input values from Table 1. Good agreement between measured and model-predicted DIF-values is obtained, see Fig. 5 (b). This underscores the linear increase of the DIF with increasing size of the specimens.

The model underestimates the DIF-values of Zhang et al., obtained with the smallest high-dynamic loading rates, see Fig. 5. An evidence-based explanation for this underestimation is out of reach, and it does not seem to be typical for the model, see its performance in the other cases studied herein.

The model of Fischer et al. [5] allows for accurate quantification of the high-dynamic strength gain of specimens subjected to uniaxial *compression*, for a variety of cementitious materials including cement pastes (Fig. 4), mortars (Fig. 5), and concretes (Fig. 3). This provides the motivation to check whether or not the *same* modeling concept also allows for quantification of the high-dynamic strength gain of specimens in case of uniaxial *tension*.

3. Analysis of high-dynamic tension tests

SHPBs were used for the high-dynamic tension tests analyzed in the present paper. The experimental setup consisted of a serial arrangement of a striker bar, an incident bar, and a cylindrical specimen, see Fig. 6. The striker bar was shot against the incident bar. The impact created a compression pulse, traveling along the incident bar. This pulse was partly transmitted and partly reflected at the interface between the incidental bar and the specimen. The transmitted compression pulse traveled along the specimen. Its reflection at the free end of the specimen created a tension pulse. The latter traveled in the opposite direction and interfered with the rest of the incoming compression pulse. The effective stress was the sum of the incoming compression pulse and the reflected tension pulse.

As for the evaluation of such high-dynamic tension tests, it is usually

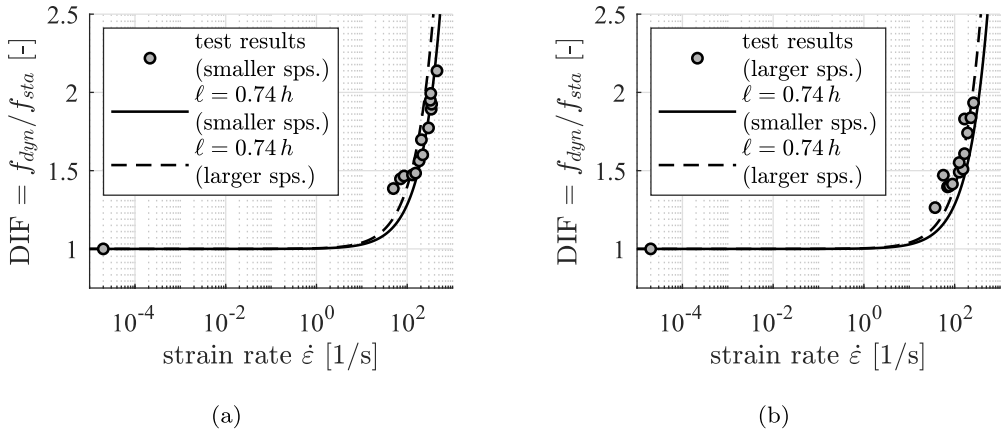

Fig. 5. High-dynamic compression tests of Zhang et al. [12] of geometrically similar mortar cylinders: measured DIF values as a function of $\dot{\varepsilon}$: (a) smaller specimens, (b) larger specimens; DIF values according to Eqs. (3)–(6) and (10) with input values listed in Table 1: the solid lines follow from a *fitting* process regarding the smaller specimens, the dashed lines illustrate *predictions* of the model for the larger specimens.

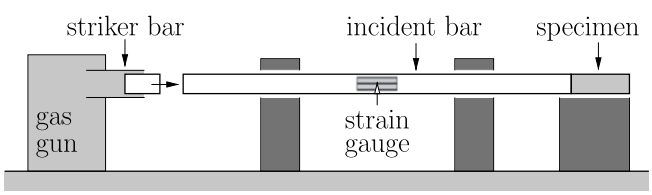

Fig. 6. Experimental setup of a Split Hopkinson Pressure Bar for a high-dynamic tension test.

assumed that the stress is uniform in every cross-section of the specimen, and that the latter is split *instantaneously* into two pieces if the most strongly loaded cross-section is subjected to a tensile stress, equal to the *high-dynamic tensile strength* of the material.

The following analysis is based on a set of *different* assumptions. An elasto-brittle analysis is carried out. It is based on wave propagation in linear-elastic, isotropic, homogeneous bars. Following the modeling approach of Fischer et al. [5], the specimens are treated as intact as long as the maximum tensile stress is smaller than the *quasi-static tensile strength*. Once the latter is reached in the most strongly loaded cross-section of the specimen, crack nucleation is envisaged. Given that the microstructure of mortars and concretes is heterogeneous, crack nucleation is assumed to occur at the point of minimum resistance in that cross-section, e.g. at the position of an interfacial transition zone around a large aggregate. In other words, it is assumed that the described cross-section does *not* break *instantaneously* into two pieces, but that local crack nucleation is followed by crack propagation in this cross-section, orthogonal to the direction of loading. The speed of the crack propagation is set equal to the velocity of shear waves, see Eq. (4). The growing crack represents an interface. Stress pulses striking this interface are reflected analogous to the reflection of waves at the free end. Stress pulses that do not strike the interface are transmitted across the intact part of the cross-section containing the crack. The high-dynamic strength gain is envisaged to occur during the period of time required for the crack to grow so large that the entire cross-section is split. Thus, the high-dynamic strength gain refers to the increase of the tensile stress, transmitted across the intact part of the cross-section where the crack is propagating.

The described hypotheses are checked against experimental data from high-dynamic strength tests by Brara and Klepaczko [7, 8] and Erzar and Forquin [13, 14], respectively. These studies were selected, because the authors provided exemplary information regarding the compression pulse transferred to the specimens. This information is required for the theoretical analysis. Notably, the two test series differ in terms of the employed measurement instrumentation and the procedures used for quantification of the high-dynamic tensile strength and the loading rate. Therefore, the two test series are analyzed in a customized fashion. Elastic wave propagation along a linear-elastic, isotropic, homogeneous bar is investigated mathematically in order to compute the quantities that were measured in the tests. The simulated quantities are then evaluated analogous to the strategy, chosen for the evaluation of the experimental measurements. This way, it can be checked whether or not the envisaged behavior of the specimens allows for explaining the experimental observations.

3.1. High-dynamic tension tests by Brara and Klepaczko

Brara and Klepaczko [7, 8] tested mortar cylinders, see Table 1 for geometric and mechanical properties of the specimens. They were drilled out of larger mortar blocks.

The incident bar of the used SHPB was equipped with three strain

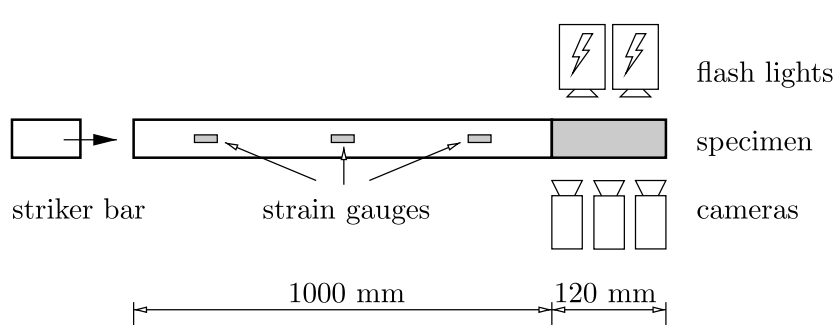

Fig. 7. Experimental setup and instrumentation used by Brara and Klepaczko [8] for high-dynamic tension tests: strain gauges were glued to the incident bar, and high-speed cameras and flash lights were positioned at opposite sides of the specimen.

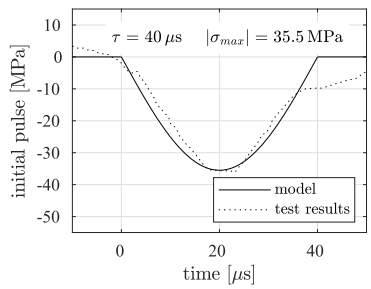

Fig. 8. Stress pulse transmitted to the specimen by Brara and Klepaczko: the dotted line illustrates measurements taken from Fig. 8 (b) of [7]; the solid line illustrates the approximation of this pulse, based on a sine function, see Eqs. (11)–(14) and (28)–(32).

gauges, see Fig. 7. Corresponding measurements regarding the incoming pulse and the reflected pulse allowed for determination of the shape, the duration, and the amplitude of the compression pulse transferred to the specimen, see Fig. 8. In addition, the instrumentation included high-speed cameras and flash lights positioned at opposite sides of the specimen, see Fig. 7. When the first crack had split the specimen, the flash lights became directly visible from the viewpoint of the cameras. This way, Brara and Klepaczko determined the time instant and the position at which the specimen had failed.

As for the evaluation of their tests, Brara and Klepaczko used wave propagation through a linear-elastic, isotropic, homogeneous bar. They determined the tensile stress and the strain rate at the time instant and at the position of failure of the specimen, see Table 1 for the test results. Thus, they assumed implicitly that the specimens remain intact up to the high-dynamic tensile strength and that the cracks propagate infinitely fast such that cracking *instantaneously* splits the specimen into two pieces, see [42] for further details.

3.2. Analysis of the high-dynamic tension tests by Brara and Klepaczko

Analytical formulae will be derived in the following. They allow for prediction of the time instant and the cross-section at which the quasi-static tensile strength is reached, and of the values of the high-dynamic tensile strength f_{dyn} and the corresponding strain rate $\dot{\varepsilon}$. Input for the analysis is the compression pulse σ_c, transferred to the specimen. The measured pulse can be approximated reasonably well as a half-wave of a sine function, see Fig. 8. Denoting the spatial and temporal variables as x and t, respectively, the mathematical formulation of σ_c reads as

$$\sigma_c(x,\,t) = -|\sigma_{max}|\,\sin\left[\frac{\pi\,(x+\xi)}{\xi} - \frac{\pi\,t}{\tau}\right]\chi_c(x,\,t), \tag{11}$$

see also the dash-dotted lines in Fig. 9. In Eq. (11), $|\sigma_{max}|$ denotes the absolute value of the maximum pressure, τ stands for the duration of the stress pulse, ξ denotes the spatial length of the pulse, and $\chi_c(x,t)$ stands for a characteristic function which ensures that the compression pulse is modeled as one half-wave rather than as an infinite number of waves. It is defined as

$$\chi_c(x,\,t) = \begin{cases} 1\cdots x \in [v_\ell\,t - \xi;\, v_\ell\,t]. \\ 0\cdots\text{otherwise}. \end{cases} \tag{12}$$

In Eq. (12), v_ℓ denotes the velocity of the longitudinal stress wave. It is equal to the velocity of a bar wave, given as

$$v_\ell = \sqrt{\frac{E}{\rho}}. \tag{13}$$

Notably, ξ, v_ℓ, and τ satisfy the condition

$$\xi = v_\ell\,\tau. \tag{14}$$

Once the incoming compression pulse reaches the free end of the specimen, see Fig. 9 (c), it is reflected as a tension pulse, $\sigma_t(x,t)$, compare Fig. 9 (c) and (d). The reflected pulse is described mathematically as a second pulse, which has the same size and shape as the one defined in Eq. (11); only the sign, the traveling direction, and the initial position (at the time instant $t = 0$) are adjusted:

$$\sigma_t(x,\,t) = |\sigma_{max}|\,\sin\left[\frac{\pi\,(2\,h - x + \xi)}{\xi} - \frac{\pi\,t}{\tau}\right]\chi_t(x,\,t) \tag{15}$$

with

$$\chi_t(x,\,t) = \begin{cases} 1\cdots x \in [2\,h - v_\ell\,t;\, 2\,h - v_\ell\,t + \xi], \\ 0\cdots\text{otherwise}, \end{cases} \tag{16}$$

see the dotted lines in Fig. 9. The two pulses interfere with each other. The effective stress σ_{eff}, acting on the material, is the sum of the incoming compression pulse and the reflected tension pulse:

$$\sigma_{eff}(x,\,t) = \sigma_c(x,\,t) + \sigma_t(x,\,t). \tag{17}$$

At the free end of the bar ($x = h$), the absolute value of the reflected tension pulse is, at all times, equal to the absolute value of the incoming compression pulse:

$$\sigma_t(h,\,t) = -\sigma_c(h,\,t). \tag{18}$$

Thus, the effective stress is, at all times, zero at the free end of the specimen, such that the stress-free boundary condition is satisfied, i.e.,

$$\sigma_{eff}(h,\,t) = 0. \tag{19}$$

Furthermore, as long as less than half of the incoming compression pulse has traveled through the specimen, the effective stress is *compressive* throughout the specimen, see Fig. 9 (d) and (e). If more than half of the compression pulse has already been reflected at the free end, effective *tensile* stresses develop at least in parts of the specimen, see Fig. 9 (g) and (h). Notably, the maximum tensile stress occurs at the position of the end of the compression pulse, see the arrows in Fig. 9 (g) and (h). This position reads as $x = v_\ell t - \xi$.

Crack nucleation is assumed if the maximum effective stress reaches the quasi-static tensile strength, i.e.

$$\max_{x,t}\,\sigma_{eff}(x,\,t) = f_{sta}. \tag{20}$$

The extreme-value problem concerned can be solved analytically, considering Eqs. (17), (11), (12), (15), and (16). The quasi-static tensile strength is reached for the first time at the time instant

$$t_c = \frac{1}{v_\ell}\left\{h + \frac{\xi}{2}\left[1 + \frac{1}{\pi}\,\arcsin\left(\frac{f_{sta}}{|\sigma_{max}|}\right)\right]\right\} \tag{21}$$

and at the position

$$x_c = h - \frac{\xi}{2}\left[1 - \frac{1}{\pi}\,\arcsin\left(\frac{f_{sta}}{|\sigma_{max}|}\right)\right]. \tag{22}$$

Crack nucleation is considered to occur at the *point* of minimum resistance within the cross-section at position x_c. Right after nucleation, the crack starts to propagate in the radial direction. The speed of the crack propagation is set equal to the velocity of shear waves, see Eq. (4). This allows for estimation of the duration of the failure process. The latter starts at the time instant of crack nucleation and ends if the crack has propagated through the entire cross-section, resulting in disintegration of the specimen. Notably, the exact location of nucleation of the crack *inside the cross-section* at the position x_c is unknown. Still, realistic scenarios must be inside the interval defined by the following two bounds:

1. If the crack nucleates at the center of the cross-section, the crack edge has to propagate along half of the diameter of the specimen. The corresponding duration of the failure process amounts to $d/(2\,v_s)$.

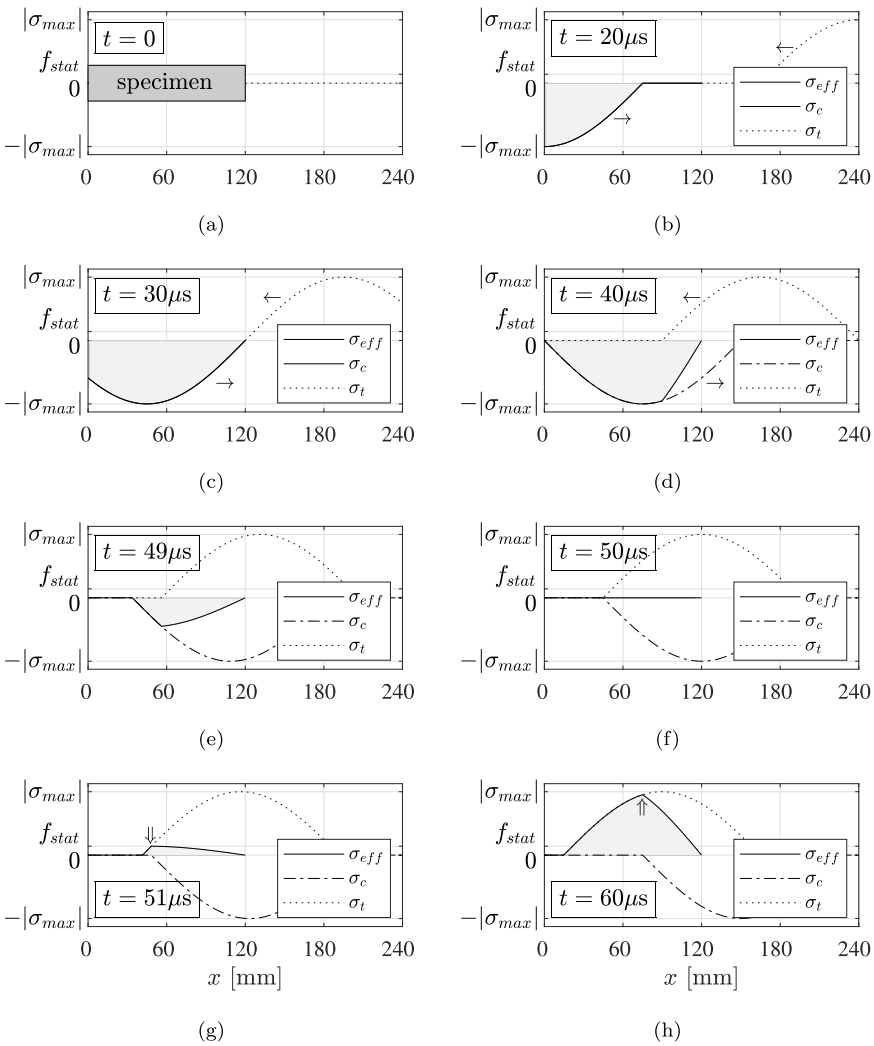

Fig. 9. Propagation of a sine-shaped pulse with $|\sigma_{max}| = 35.5$ MPa and $\tau = 40$ μs along the axis of a linear-elastic, isotropic, homogeneous bar of axial length h = 120 mm: (a) $t = 0$ μs: illustration of the position of the specimen; (b) $t = 20$ μs: the compression pulse has entered the specimen; (c) $t = 30$ μs: the compression pulse has reached the free end of the specimen; (d) $t = 40$ μs: the compression pulse is already partly reflected at the free end, but the effective stress is still compressive throughout the specimen; (e) $t = 49$ μs: the effective compressive stresses have decreased significantly; (f) $t = 50$ μs: the peak of the compression pulse has reached the free end of the specimen; the effective stresses vanish; (g) $t = 51$ μs: crack nucleation; (h) $t = 60$ μs: effective stresses are tensile throughout the specimen.

2. If the crack nucleates at the outer contour of the cross-section, the crack edge has to propagate across the entire diameter of the specimen. The corresponding duration of the failure process amounts to d/v_s.

The time instant of failure of the specimen, t_f, is equal to the sum of t_c according to Eq. (21) and the duration of the failure process, see the two items above. Thus, t_f satisfies the following inequalities

$$t_c + \frac{d}{2\,v_s} \leq t_f \leq t_c + \frac{d}{v_s}. \tag{23}$$

In the time interval $[t_c; t_f]$, the growing crack represents an interface. Stress pulses striking this interface are reflected analogous to the reflection of waves at the free end. Stress pulses that do not strike the interface are transmitted across the intact part of the cross-section containing the crack. For this intact part, the expression of the effective stress according to Eq. (17) remains valid. The high-dynamic tensile strength of the tested specimen is understood as the tensile stress which is transmitted across the last bridge of material, right before the analyzed cross-section is split entirely by the crack. Thus, f_{dyn} is obtained as the effective stress according to the Eqs. (17), (11), (12), (15), and (16), evaluated for the cross-section at the position x_c according to Eq. (22), at the time instant of failure, t_f, according to the inequalities (23). The upper bound of t_f yields

$$f_{dyn} \geq |\sigma_{max}| \sin\left[\frac{d}{v_s}\frac{\pi}{\tau} + \arcsin\left(\frac{f_{sta}}{|\sigma_{max}|}\right)\right], \tag{24}$$

whereas the lower bound of t_f gives

$$f_{dyn} \leq |\sigma_{max}| \sin\left[\frac{d}{2v_s}\frac{\pi}{\tau} + \arcsin\left(\frac{f_{sta}}{|\sigma_{max}|}\right)\right]. \tag{25}$$

The loading rate associated with f_{dyn} is determined analogous to the strategy used by Brara and Klepaczko for the evaluation of their tests. Following the scheme used for the evaluation of the experiments, the stress rate at failure is computed as the dynamic strength divided by the duration of tensile loading

$$\dot{\sigma} = \frac{f_{dyn}}{t_f - t_0}, \tag{26}$$

where t_0 denotes the time instant at which the effective stress of the position x_c turns from compression to tension. In order to quantify t_0, Eqs. (11), (12), (15), and (16) are inserted into Eq. (20). The resulting expression is specialized for $x = x_c$ according to Eq. (22) and for $\sigma_{eff} = 0$. The obtained expression is then solved for t. This delivers

$$t_0 = t_c - \frac{\tau}{2\,\pi}\arcsin\left(\frac{f_{sta}}{|\sigma_{max}|}\right). \tag{27}$$

Finally, the strain rate $\dot{\varepsilon}$ is computed based on the assumption of linear-elastic material behavior, see Eq. (6).

Concerning the numerical evaluation of the analytical formulae

according to the Eqs. (11)–(27), the stress pulse illustrated in Fig. 8 is modeled based on

$$|\sigma_{max}| = 35.5 \text{ MPa}, \tag{28}$$

$$\tau = 40\ \mu\text{s}. \tag{29}$$

In addition, Brara and Klepaczko provided values of f_{sta}, E, ν, and ρ of the tested material, see Table 1. Thus, v_s and v_ℓ follow from Eqs. (4) and (13) as

$$v_s = 2413 \text{ m/s}, \tag{30}$$

$$v_\ell = 3754 \text{ m/s}. \tag{31}$$

The value of ξ follows from inserting Eqs. (31) and (29) into Eq. (14) as

$$\xi = 150 \text{ mm}. \tag{32}$$

The corresponding values of the dynamic tensile strength and the strain rate are obtained based on the derived analytical formulae (11)–(27). If cracking started at the center of the cross-section, the model yields

$$f_{dyn} = 16.0 \text{ MPa}, \qquad \dot{\varepsilon} = 51.1/\text{s}, \tag{33}$$

see the white circle in Figs. 10 and 11 (a). If cracking started at the outer contour of the cross-section, the model gives

$$f_{dyn} = 25.3 \text{ MPa}, \qquad \dot{\varepsilon} = 44.4/\text{s}, \tag{34}$$

see the white square in Figs. 10 and 11 (a). From comparison of these model-predictions with experimental data, it is concluded that cracking has started most likely at the outer contour of the cross-section.

In order to simulate other rates of loading, the stress pulse must be modified. This is the motivation to carry out a sensitivity analysis regarding τ, while $|\sigma_{max}|$ remains equal to 35.5 MPa and cracking is assumed to start at the outer contour of the cross-section. The resulting model predictions explain the experimental data quite well, see Fig. 11 (a). Still, a stress pulse with $|\sigma_{max}| = 35.5$ MPa can only explain high-dynamic strength values up to 35.5 MPa. Two experimentally measured strength values are larger than 35.5 MPa, see Table 1 and the two data points at the top of the diagram in Fig. 11 (a). It is concluded that at least some of the tests of Brara and Klepaczko were carried out with a stronger stress pulse. In [43], the authors mention stress pulses with maximum intensities of 35.5 MPa and 58.0 MPa, respectively. This provides the motivation to set $|\sigma_{max}| = 58.0$ MPa and to perform a sensitivity analysis regarding τ, while cracking is assumed to start at the outer contour of the cross-section. The resulting model predictions again explain the experimental data quite well, including the two data points that were out of reach, based on $|\sigma_{max}| = 35.5$ MPa, compare Fig. 11 (a) and (b). This corroborates the usefulness of the underlying modeling approach.

In SHPB-testing, the stress peak is the larger, the faster the impactor, and the duration of the stress pulse is the longer, the longer the impactor. However, details regarding the projectiles used by Brara and Klepaczko are unknown. This provided the motivation to carry out sensitivity analyses regarding the maximum intensity and the duration of the stress pulse.

3.3. High-dynamic tension tests by Erzar and Forquin

Erzar and Forquin [13, 14] tested concrete cylinders, see Table 1 for geometric and mechanical properties of the specimens. They were drilled out of larger concrete blocks.

The lateral surface of each specimen was equipped with three strain gauges (Fig. 12). Their readings provide access to the strain rates at three positions at the surface of the specimen. The strain measurements also allowed for characterization of the incoming compression pulse in terms of its shape, duration, traveling velocity, and amplitude, see Fig. 13. A laser interferometer was used to measure the axial velocity of the free end of the tested specimens, $v(h,t)$, see Fig. 14.

Concerning the evaluation of the tests, the dynamic tensile strength was computed based on the Novikov formula [44]

$$f_{dyn} = [\max_t v(h,t) - \min_t v(h,t)]\frac{\rho\, v_\ell}{2}, \tag{35}$$

where $\max_t v(h,t)$ and $\min_t v(h,t)$ denote measured values of the maximum and of the following local minimum of the axial velocity of the free end of the specimens. As for theoretical basics of the Novikov formula, see Appendix A. The formula is exemplarily illustrated in Appendix B.

In order to determine the corresponding strain rate, the authors applied the following procedure to the individual readings of the strain gauges attached to the specimen. The strain readings were converted into stress histories based on Hooke's law in order to determine the time instant at which f_{dyn} was reached. Returning to the strain measurements, the strain rate was quantified at that time instant. This procedure delivered one value of the strain rate from each of the strain gauges. These values were averaged among the strain gauges in the vicinity of the macrocrack that had split the specimen. This average strain rate was assigned to f_{dyn}, see Table 1 for the test results and [13] for further details.

3.4. Analysis of the high-dynamic tension tests by Erzar and Forquin

In the following, the usefulness of the proposed modeling approach concerning reproduction of the experimental results of Erzar and Forquin [13] will be checked. To this end, the relationship between the particle velocity at the free end of the specimen and the intensity of the compression pulse striking this free end is used:

$$v(h,t) = -\frac{2\,\sigma_c(h,t)}{\rho\, v_\ell}. \tag{36}$$

Eq. (36) can be derived considering wave propagation in a linear-

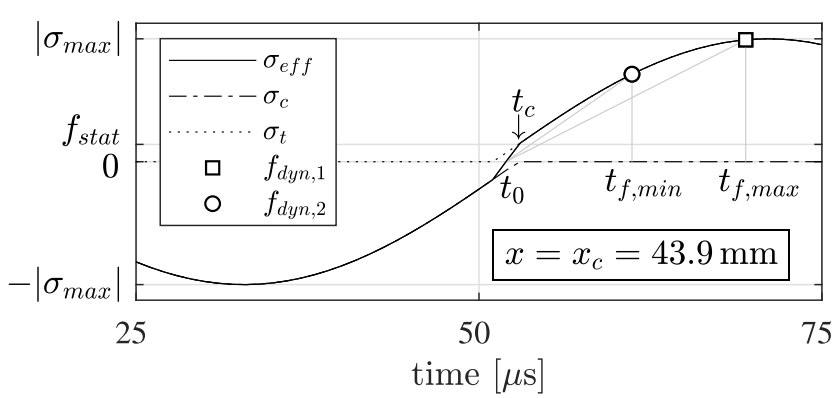

Fig. 10. Evolution of the effective stress at the cross-section affected by cracking.

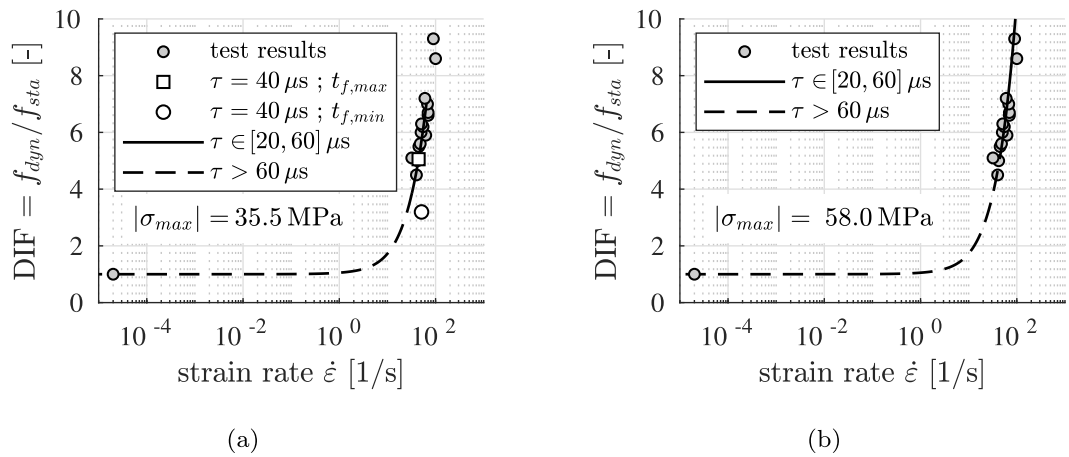

Fig. 11. Test results from Brara and Klepaczko [7, 8], see the gray circles, and model-predicted dynamic tensile strength values as a function of the strain rate, quantified on the basis of Eqs. (11)–(27), see the lines: (a) $|\sigma_{max}|$ = 35.5 MPa and (b) $|\sigma_{max}|$ = 58.0 MPa.

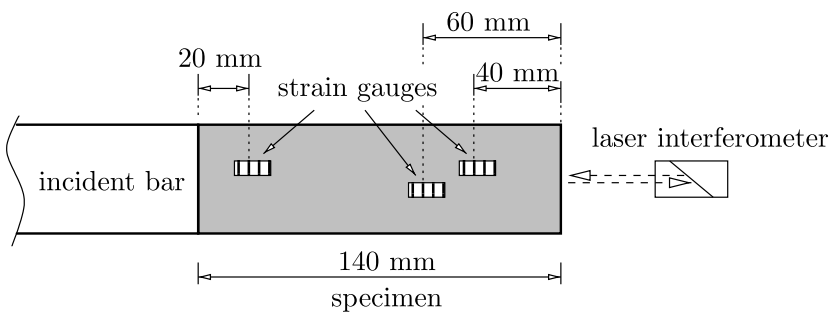

Fig. 12. Experimental setup and instrumentation used by Erzar and Forquin [13, 14] for high-dynamic tension tests: strain gauges were glued onto the surface of the specimen, and a laser interferometer measured the axial velocity of the free end of the specimen.

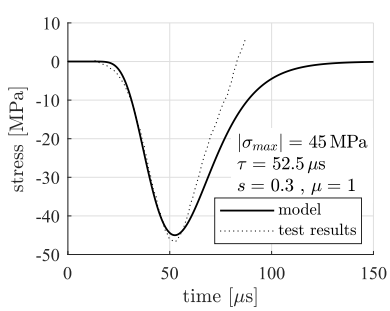

Fig. 13. Experimental measurements and approximation of the stress pulse transferred to one of the tested specimens, based on a log-normal function, see Eqs. (37)–(43).

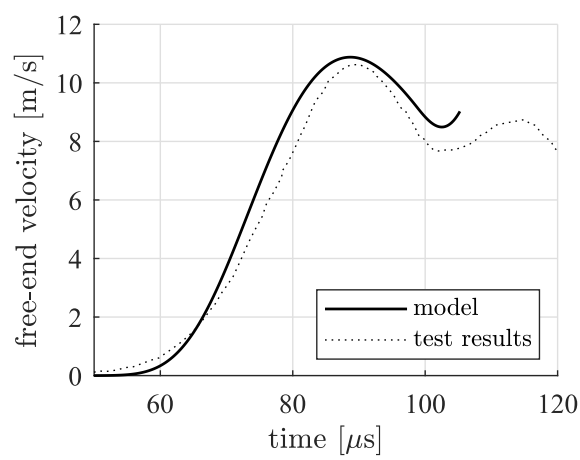

Fig. 14. Experimental measurements and model-predicted evolution of the axial velocity of the free end of the specimen, computed by means of Eqs. (36)–(56).

elastic, isotropic, homogeneous bar, see Appendix A.2.

Notably, the Novikov formula (35) requires consideration of non-symmetric pulses, see Appendix B. Therefore, the stress pulse transferred to the specimen is approximated based on a log-normal function which is normalized such that its maximum value is equal to +1:

$$f(p) = \frac{1}{p} \exp\left(-\frac{[\ln(p) - \mu]^2 + s^2\,(s^2 - 2\,\mu)}{2\,s^2}\right), \tag{37}$$

where μ and s will be chosen suitably in order to adjust the shape of the modeled stress pulse to the available measurement data, see Fig. 13. The maximum of the function (37) is located at the position

$$p = p_{max} = \exp\,(\mu - s^2). \tag{38}$$

The mathematical formulation of the incoming compression pulse reads as

$$\sigma_c(x,\,t) = -|\sigma_{max}|\,f\left(p = \left[\frac{t}{\tau} - \frac{x}{\xi}\right] p_{max}\right), \qquad x < v_\ell\,t, \tag{39}$$

where τ is equal to the period of time from the beginning of the pulse until its maximum is reached, see Fig. 13. The corresponding spatial distance is denoted as ξ. It is related to τ via Eq. (14). Concerning the approximation of the stress pulse measured by Erzar and Forquin [13], the following input values are used

$$\mu = 1.0, \tag{40}$$

$$s = 0.3, \tag{41}$$

$$|\sigma_{max}| = 45 \text{ MPa}, \tag{42}$$

$$\tau = 52.5\ \mu\text{s}, \tag{43}$$

see Fig. 13. In addition, Erzar and Forquin provided values of f_{sta}, E, ν, and ρ of the tested material, see Table 1. Thus, v_s and v_ℓ follow from Eqs. (4) and (13) as

$$v_s = 2461 \text{ m/s}, \tag{44}$$

$$v_\ell = 3868 \text{ m/s}. \tag{45}$$

Inserting Eqs. (45) and (43) into Eq. (14) yields the value of ξ as

$$\xi = 203 \text{ mm}. \tag{46}$$

The incoming compression pulse is reflected at the free end of the specimen as a tension pulse. It reads as

$$\sigma_t(x, t) = +|\sigma_{max}| f\left(p = \left[\frac{t}{\tau} + \frac{x - 2h}{\xi}\right] p_{max}\right), \qquad x > 2h - v_\ell t. \tag{47}$$

Superposition of the incoming compression pulse, see Eq. (39), and the reflected tension pulse, see Eq. (47), yields the effective stress, see Eq. (17). The latter satisfies the stress-free boundary condition at the free end of the specimen.

A crack is assumed to nucleate if the effective stress reaches the quasi-static strength at the most strongly loaded cross-section of the specimen, i.e.,

$$\sigma_{eff}(x_c, t_c) = f_{sta}. \tag{48}$$

The time instant t_c and the location of the cross-section, x_c, where cracking starts, are obtained as

$$t_c = 90.8\ \mu\text{s}, \tag{49}$$

$$x_c = 109 \text{ mm}. \tag{50}$$

Crack nucleation is considered to occur at the *point* of minimum resistance within the cross-section at position x_c. Right after nucleation, the crack starts to propagate in the cross-section. The growing crack represents an interface. Stress pulses striking this interface are reflected analogous to the reflection of waves at the free end. Stress pulses that do not strike the interface are transmitted across the intact part of the cross-section containing the crack. This provides the motivation to quantify the increasing crack area, $A_c(t)$. Assuming that cracking starts at the center of the cross-section and that the crack edge propagates at the speed v_s, $A_c(t)$ is obtained as

$$A_c(t) = [(t - t_c)\, v_s]^2\, \pi. \tag{51}$$

Eq. (51) is valid for all time instants within the following interval:

$$t_c \le t \le t_c + \frac{d}{2\, v_s}. \tag{52}$$

In order to predict the velocity of the free end of the specimen, the following analysis focuses on pulses traveling inside the spatial domain between the crack and the free end of the specimen.

1. At any time t, satisfying Eq. (52), the incoming compression pulse passes through the intact part of the cross-section containing the crack. This part is equal to $A - A_c(t)$, where A denotes the entire cross-sectional area. The transmitted pulse continues to be a compression pulse which travels towards the free end, see the gray solid lines in Fig. 15.
2. At the same time t, also the reflected tension pulse partly strikes the crack area $A_c(t)$ from the opposite side, and it is again reflected. It turns into a compression pulse which travels to the free end, see the black dashed lines in Fig. 15.

The time in which the two signals need to cover the distance from the cracked cross-section ($x = x_c$) to the free end ($x = h$) amounts to $[h - x_c]/v_\ell$. Force balance [45] gives access to the average stress, σ, arriving at time instant $t + [h - x_c]/v_\ell$ at the free end:

$$\sigma(h, t + [h - x_c]/v_\ell)\cdot A = \sigma_c(x_c, t)\cdot[A - A_c(t)] - \sigma_t(x_c, t)\cdot A_c(t), \tag{53}$$

where the minus sign on the right-hand-side of Eq. (53) accounts for the compressive nature of the tension pulse reflected at the crack surface. Notably, Eq. (53) is valid in the time interval defined in Eq. (52).

Summarizing, the velocity of the free end of the specimen is predicted as follows: At first, the signal arriving at the free end of the specimen is the one of the incoming compression pulse, see Eq. (39). Thus, $\sigma(h,t)$ in Eq. (36) reads as

$$\sigma(h, t) = -|\sigma_{max}| f\left(p = \left[\frac{t}{\tau} - \frac{h}{\xi}\right] p_{max}\right). \tag{54}$$

The limit of applicability of Eq. (54) is reached if a signal that is influenced by the crack arrives at the free end. Thus, Eq. (54) is valid for values of t, satisfying

$$0 \le t \le t_c + \frac{h - x_c}{v_\ell}. \tag{55}$$

Thereafter, Eq. (53) is valid. It can be re-arranged and transformed into

$$\sigma(h, t) = \sigma_c\left(x_c, t - \frac{h - x_c}{v_\ell}\right)\cdot\left[1 - \frac{A_c\left(t - \frac{h - x_c}{v_\ell}\right)}{A}\right] - \sigma_t\left(x_c, t - \frac{h - x_c}{v_\ell}\right)\cdot\frac{A_c\left(t - \frac{h - x_c}{v_\ell}\right)}{A}. \tag{56}$$

Eq. (56) is valid in the time interval

$$t_c + \frac{h - x_c}{v_\ell} \le t \le t_c + \frac{3\,(h - x_c)}{v_\ell}. \tag{57}$$

During this period of time, a local minimum of the velocity of the free end of the specimen is observed, see Fig. 14.

The simulated quantities are post-processed analogous to the strategy used by Erzar and Forquin to evaluate their measurements. Inserting the extreme values of the model-predicted velocity, $\max_t v(h, t) = 10.8$ m/s and $\min_t v(h, t) = 8.5$ m/s, into the Novikov formula (35), delivers

$$f_{dyn} = 10.4 \text{ MPa}, \tag{58}$$

see the ordinate of the white square in Fig. 16. The spatio-temporal function of the strain rate is obtained with the help of Hooke's law, see Eq. (6), as

$$\dot{\varepsilon}(x, t) = \frac{\dot{\sigma}_{eff}(x, t)}{E}. \tag{59}$$

The value of the strain rate associated with f_{dyn} is determined by analogy to the strategy used by the experimentalists for the evaluation of their test results. It is computed as the average of the strain rates, obtained at the positions of the two strain gauges in the vicinity of the cracked cross-section, at the time instants when the dynamic strength is reached at these positions:

$$\dot{\varepsilon} = \frac{\dot{\varepsilon}(80 \text{ mm}, t_1) + \dot{\varepsilon}(100 \text{ mm}, t_2)}{2}, \tag{60}$$

where t_1 and t_2 are implicitly defined as

$$\sigma_{eff}(80 \text{ mm}, t_1) = \sigma_{eff}(100 \text{ mm}, t_2) = f_{dyn}. \tag{61}$$

As for the stress pulse illustrated in Fig. 13, this approach yields

$$\dot{\varepsilon} = 79/\text{s}. \tag{62}$$

The model-predicted values of f_{dyn} and $\dot{\varepsilon}$, see Eqs. (58) and (62), are

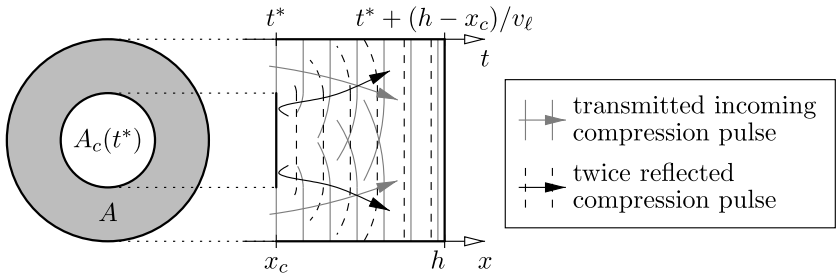

Fig. 15. Schematic illustration of wave fronts: the gray solid lines show the wave front of the part of the incoming compression pulse that passes, at time t^*, through the intact part of the cracked cross-section; the black dashed lines show the wave front of the part of the reflected tension pulse that strikes the crack at time t^*.

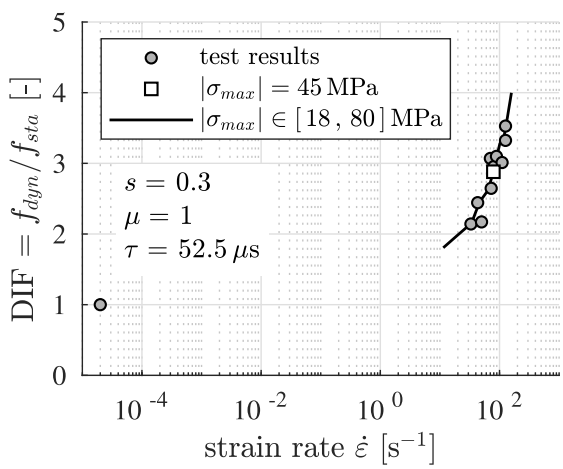

Fig. 16. Test results of Erzar and Forquin [14], see the gray circles, and model-predicted values of the dynamic tensile strength as a function of the strain rate, computed by means of Eqs. (35)–(60), see the solid line.

within the cloud of data of the test results of Erzar and Forquin, see the white square in Fig. 16.

The other test results can be explained by means of sensitivity analysis where $|\sigma_{max}|$ is varied and all other input quantities are kept constant, see the solid line in Fig. 16. This further corroborates the underlying modeling approach.

Crack nucleation was envisaged at the center of the cross-section, see point P1 in Fig. 17. It is interesting to note that the underlying expression for $A_c(t)$ according to Eq. (51) remains valid as long as the crack nucleated in a circular region around the center of the cross-section, whereby the radius of this region amounts to 0.59-times the radius of the tested specimen, see the shaded regions in Fig. 17. This can be explained as follows: The minimum of the free-end velocity illustrated in Fig. 14 refers to the arrival of a stress pulse which contains a contribution from the tension wave reflected at the crack, at the time t^* when the crack radius is equal to 0.41-times the radius of the tested specimen. Even if the crack nucleated at the boundary of the described region, see e.g. point P2 in Fig. 17, and started to propagate in a radial-symmetric fashion, Eq. (51) and the derivation leading to Eqs. (58) and (62) remain valid. The analysis of crack nucleation at the outer contour of the cross-section (or close to it) would significantly increase the complexity of the function $A_c(t)$ according to Eq. (51).

4. Discussion

The following discussion elucidates the difference between a "material" and a "structural" strength value, the interpretation of "strength" values obtained from both quasi-static and high-dynamic testing, and the potential and limitations of the presented model.

The "strength of a material", is a property of representative volume elements (RVEs). As regards concrete, the characteristic size of the RVEs is by a factor of at least 2 to 3 larger than the characteristic size of the aggregates [46]. The markedly heterogeneous microstructure of concrete entails a fluctuating microscopic strength distribution. The weakest domains of the microstructure of normal concrete are the ITZs covering the aggregates [47, 48]. The characteristic thickness of the ITZs ranges from 15 μm to 30 μm [49]. The aggregates and the cement paste matrix, in turn, are significantly stronger than the ITZs. This was the motivation to assume that (i) the first crack nucleates at the point of minimum resistance in the most strongly loaded cross-section, once the tensile stress has reached the quasi-static strength, and (ii) subsequent crack propagation is restricted to this cross-section.

The larger the size of an RVE of concrete, the larger the probability to find a microscopic domain within the RVE, at which the strength is particularly small. However, this statistical size effect [50] is *in*significant when comparing strength values of specimens used for laboratory testing, with characteristic sizes ranging from several centimeters to a few decimeters. Thus, the *material strength* of concrete is virtually independent of the size of the tested RVE.

Quasi-static and high-dynamic testing can be distinguished based on

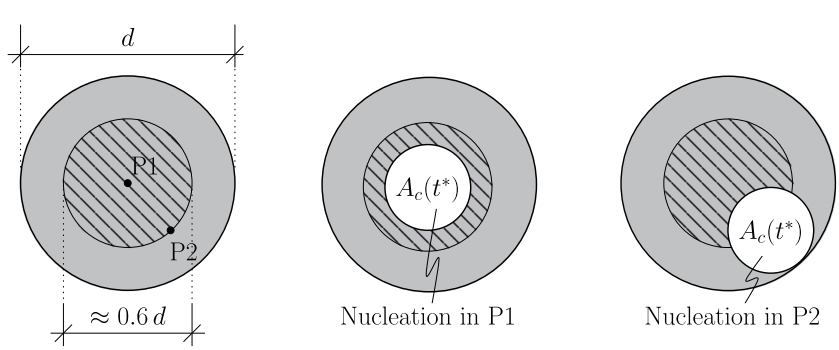

Fig. 17. Region where the first crack may nucleate such that the expression for $A_c(t)$ according to Eq. (51) remains valid for re-analysis of the high-dynamic tension test by Erzar and Forquin [14].

the following arguments concerning separation or similarity of time scales.

- A *quasi-static* strength test lasts by orders of magnitude longer than the failure process of the specimen, which spans from crack nucleation at the spot of minimum microstructural resistance to disintegration of the specimen. Because the loading is increased relatively slowly and crack propagation is relatively fast, the loading cannot be increased significantly during the failure process. Consequently, the "quasi-static strength" is virtually independent of the size of the specimen. This is the rationale for the expression "quasi-static material strength of concrete".
- The duration of a *high-dynamic* strength test is of the same order of magnitude as the characteristic duration of the failure process of the specimen. Because the loading is increased similarly fast as the crack propagation process, it can be increased significantly during the failure process. Considering that cracks propagate at a speed which is characteristic for the tested material, the period of time, ranging from crack nucleation to final disintegration of the specimen, is the longer, the larger the spatial dimensions of the specimen. Thus, the increase of the stress during the failure process (= "the high-dynamic strength gain") is the larger, the larger the size of the specimen. This line of arguments underscores that the "high-dynamic strength" depends on the size of the specimen. This is the rationale for the expression "high-dynamic structural strength of a concrete specimen".

The presented model was designed to be as simple as possible and just as complex as necessary. Focusing on expected first-order effects, phenomena of secondary importance were not considered. In the following, current limitations of the model and the corresponding potential for future extensions are discussed:

- The presented model is restricted to the first crack. During propagation of this crack, the model envisages that the stress increases in the remaining intact parts of the specimen. This renders it likely that additional cracks nucleate at other positions in the specimen. This line of argumentation implies that a high-dynamically loaded specimen finally disintegrates into many small pieces, which is consistent with experimental observations, see e.g. [5, 51]. Still, the additional cracks were not explicitly accounted for in the presented approach.
- Possible confinement resulting from inertia effects and possible strain-rate-dependent material behavior resulting from the viscoelastic character of cement paste were not considered. As regards viscoelasticity, the success of the model could be linked to the fact that dry cementitious materials exhibit a significantly smaller creep activity compared to water-saturated cementitious materials, see Fig. 1 of [52].
- Because cracking consumes energy, the intensity of the wave reflected at the crack is actually slightly smaller than considered in the presented model. The stress pulse striking the free end of the specimen is also slightly smaller than the one considered in the presented model, provided that the stress pulse contains a contribution which stems from the reflection of the tension pulse at the crack. This implies that the minimum of the free-end velocity, visible in the vicinity of $t = 100\ \mu s$ in Fig. 14, would come slightly later, and the minimum free-end velocity would be slightly smaller if energy dissipation resulting from cracking had been accounted for. In that case, the evolution of the modeled free-end velocity would be even closer to the experimental observations. This provides the motivation for the future extension of the presented model.
- The reflection of a stress pulse at a growing crack results in a problem of three-dimensional wave propagation, see the curved lines in Fig. 15. For the sake of simplicity, it was assumed that both the tension pulse reflected at the crack and the incoming compression pulse passing through the intact part of the cracked cross-section arrive, in a well intermixed fashion, as a quasi-one-dimensional wave at the free end. In order to further improve the level of detail of the analysis, it will be interesting to carry out three-dimensional simulations of wave propagation in the future.
- State-of-the-art wave propagation analysis in a SHPB setup involves consideration of wave elongation due to dilatation and dispersion, see e.g. [51, 53]. Wave elongation results in a larger duration of the stress pulse and a lower maximum amplitude. The elongation phenomenon is particularly important in the long incidental bar. Inside the relatively short specimen, in turn, wave elongation is of less importance. Thus, the presented re-analyses of high-dynamic tension tests are realistic, because they were based on stress pulses transferred to the specimens, exemplarily provided by the experimenters. In addition, the sensitivity of the presented model with respect to the maximum amplitude and the duration of the stress pulse was investigated. Results from these sensitivity analyses provide at least qualitative insight into the uncertainty associated with the wave elongation phenomenon.

5. Conclusions

Based on the results obtained from revisiting high-dynamic *compression* tests, the following conclusions are drawn:

- The high-dynamic strength tests by Kühn et al. [15] were re-analyzed based on known values of the quasi-static strength, two independent elastic stiffness constants, the mass density of the tested material, and the size of the cylindrical specimens. The unknown length of the crack propagation was treated as an optimization variable. The obtained optimal value agrees well with photos showing the fragments of specimens after testing.
- The usefulness of the model was further corroborated by analyzing high-dynamic compression tests on cement paste cylinders, performed by Fischer et al. [5]. Again, the length of crack propagation was unknown. The identified optimum value of this length is realistic, because it is located inside of an interval with two natural bounds. They describe that the first crack nucleates somewhere between the center of the specimen and its boundary where it is in contact with the load plate.
- The usefulness of the model was also corroborated for high-dynamic compression tests of two geometrically similar sets of mortar specimens, performed by Zhang et al. [12]. The length of crack propagation was identified for the set of smaller specimens. Its optimum value satisfies the aforementioned bounds, *and* it allows for *predicting* the high-dynamic behavior of the set of larger specimens. This underlines that the DIF increases indeed linearly with the size of the tested specimen, as assumed in the model. It is concluded that the high-dynamic strength gain is a structural rather than a material effect.

Based on the results obtained from analyzing high-dynamic *tension* tests, the following conclusions are drawn:

- The high-dynamic tensile strength of a concrete specimen tested by Brara and Klepaczko [7, 8] could be reproduced, because the quasi-static strength, two independent elastic stiffness constants, the mass density of the tested material, the size of the cylindrical specimen, and the incoming compression pulse were provided by the experimenters. In order to render an analytical analysis of the problem possible, the incoming compression pulse was approximated based on a sine half wave that matches the beginning and the maximum value of the pulse reasonably well, see Fig. 8. The other experimentally obtained strength values could be explained by scaling the duration and the amplitude of the sine-shaped incoming compression pulse. It is concluded that the proposed modeling approach

agrees with the experimental observations of Brara and Klepaczko [7, 8].

- The high-dynamic tensile strength of a mortar specimen tested by Erzar and Forquin [14] could be reproduced, because all input values of the model (see the listing in the previous item) were provided by the experimenters. In order to be able to follow the evaluation strategy of the authors, including the application of the Novikov formula, the incoming compression pulse was approximated based on a *non-symmetric* log-normal function which matches the beginning and the maximum value of the pulse reasonably well, see Fig. 13. The other tests were explained by scaling the amplitude of the log-normal-shaped incoming compression pulse. It is concluded that the proposed modeling approach agrees with the experimental observations of Erzar and Forquin [14].

Thus, the analysis of five campaigns of high-dynamic compression *and* tension tests of dry cementitious materials, carried out at five different laboratories, enabled validation of the following hypotheses of the proposed modeling approach:

- Also under high-dynamic loading, cracking starts if the quasi-static strength of the tested *material* is reached.
- The high-dynamic strength gain represents the increase of the stress *during* the failure process of the tested specimen, lasting from the start of crack propagation to disintegration of the specimen.

As for general structures subjected to high-dynamic loading, the following conclusions are drawn:

- If the dynamic stress exceeds the quasi-static strength at a point of a structure, local damage will occur, no matter how fast the stress increases and how short the stress pulse lasts.
- Modeling requires explicit transient simulations of crack propagation at a realistic finite speed.

List of symbols

A	cross-sectional area of the specimen
A_c	crack area
DIF	Dynamic Strength Increase Factor
d	diameter of a cylindrical specimen
E	Young's modulus
f	probability density function of a log-normal distribution, normalized such that its maximum value is equal to + 1
f_{dyn}	high-dynamic strength (in compression or in tension)
$f_{dyn,1}$	upper bound of f_{dyn}
$f_{dyn,2}$	lower bound of f_{dyn}
f_{sta}	quasi-static strength (in compression or in tension)
h	axial length of a cylindrical specimen
i	imaginary unit
ITZ	interfacial transition zone
k	wave number
ℓ	crack propagation length
$\ell_{\ell b}$	lower bound of ℓ
ℓ_{ub}	upper bound of ℓ
p	variable of the function f
p_{max}	position of the maximum value of the function f
s	parameter of the function f, referring to the standard deviation of the natural logarithm of p
t	temporal variable
t_c	time instant when the quasi-static strength is reached
t_f	time instant of failure
$t_{f,min}$	value of t_f referring to $f_{dyn,2}$
$t_{f,max}$	value of t_f, referring to $f_{dyn,1}$
t_0	time instant at which the effective stress turns from compression to tension at the position x_c
u	displacement component in the axial direction (x-direction)
v	particle velocity in the x-direction
v_s	shear wave velocity
v_ℓ	bar wave velocity
x	spatial variable in the axial direction
x_c	position at which the first crack nucleates
Δt	time increment
$\Delta t_{failure}$	duration of failure process
$\dot{\varepsilon}$	strain rate
ε_{xx}	normal strain in the axial direction (x-direction)
ε_{yy}	normal strain in the y-direction
ε_{zz}	normal strain in the z-direction
μ	parameter of the function f, referring to the mean of the natural logarithm of p
ν	Poisson's ratio
ξ	spatial length of the pulse
ρ	mass density
$\dot{\sigma}$	stress rate
σ_c	compression pulse
σ_{eff}	effective stress
$\lvert\sigma_{max}\rvert$	absolute value of the maximum of the stress pulse
σ_t	tension pulse
σ_{xx}	normal stress in the axial direction (x-direction)
$\hat{\sigma}_{xx}$	continuous spectrum of frequencies of the stress wave σ_{xx}
τ	duration of the stress pulse
χ_c	characteristic function of the compression pulse
χ_t	characteristic function of the tension pulse

Acknowledgments

Financial support by the Austrian Science Fund (FWF), provided within project P 281 31-N32 “Bridging the Gap by Means of Multiscale Structural Analyses”, is gratefully acknowledged.

Appendix A. Fundamentals of wave propagation in linear-elastic, isotropic, homogeneous bars

A.1. Relation between stress and particle velocity

Consider wave propagation along the x-axis of a bar made of a linear-elastic, isotropic, homogeneous material. The normal stress in the axial direction, σ_{xx}, is the only non-vanishing stress component. The stress wave can be formulated mathematically as the Fourier back-transform of a continuous spectrum of frequencies, $\hat{\sigma}_{xx}(k)$, as

$$\sigma_{xx}(x, t) = \int_{-\infty}^{\infty} \frac{1}{\sqrt{2\pi}} \hat{\sigma}_{xx}(k) \exp^{ik(x-v_\ell t)} \mathrm{d}k, \tag{A1}$$

where k is the wave number and i stands for the imaginary unit. The non-vanishing components of the linearized strain tensor follow from Hooke's law as

$$\varepsilon_{xx}(x,\,t) = \frac{1}{E}\int_{-\infty}^{\infty}\frac{1}{\sqrt{2\pi}}\,\hat{\sigma}_{xx}(k)\,\exp^{ik(x-v_\ell t)}\,\mathrm{d}k, \tag{A2}$$

and $\varepsilon_{yy}(x,t) = \varepsilon_{zz}(x,t) = -\nu\ \varepsilon_{xx}(x,t)$. Notably, ε_{xx} is equal to the partial derivative of the displacement component in the axial direction, u, with respect to x, i.e., $\varepsilon_{xx} = \partial u/\partial x$. Thus, spatial integration of Eq. (A2) with respect to x yields

$$u(x,\,t) = \frac{1}{E}\int_{-\infty}^{\infty}\frac{1}{\sqrt{2\pi}}\,\hat{\sigma}_{xx}(k)\,\exp^{ik(x-v_\ell t)}\,\frac{1}{ik}\mathrm{d}k. \tag{A3}$$

The particle velocity in the x-direction, v, is obtained as $v = \partial u/\partial t$. Thus, the time-derivative of Eq. (A3) yields

$$v(x,\,t) = -\frac{v_\ell}{E}\int_{-\infty}^{\infty}\frac{1}{\sqrt{2\pi}}\,\hat{\sigma}_{xx}(k)\,\exp^{ik(x-v_\ell t)}\,\mathrm{d}k, \tag{A4}$$

where v_ℓ is equal to the bar wave velocity, see Eq. (13). Comparing Eqs. (A1) and (A4) results in

$$v(x,\,t) = -\frac{v_\ell}{E}\,\sigma_{xx}(x,\,t), \tag{A5}$$

which can be reformulated, based on Eq. (13), as

$$v(x,\,t) = -\frac{\sigma_{xx}(x,\,t)}{v_\ell\,\rho}. \tag{A6}$$

A.2. Interference of a compression pulse and a reflected tension pulse

Consider that a compression pulse $\sigma_c < 0$ is reflected as a tension pulse $\sigma_t > 0$ at the free end of a bar. Because σ_c and σ_t exhibit *opposite mathematical signs*, and because the two pulses travel in *opposite directions*, the particle velocities, resulting from the two pulses, point in *the same* direction. In other words, interference of the two waves results in a mutual *amplification* of the particle velocities [54]. Thus, Eq. (A6) can be formulated as

$$v(x,\,t) = -\frac{\sigma_c(x,\,t) - \sigma_t(x,\,t)}{v_\ell\,\rho}. \tag{A7}$$

Specializing Eq. (A7) for the free end of the bar, i.e., for $x = h$, and inserting the expression for $\sigma_t(h,t)$ according to Eq. (18) into the resulting expression, yields the particle velocity at the free end as

$$v(h,\,t) = -\frac{2\,\sigma_c(h,\,t)}{v_\ell\,\rho}. \tag{A8}$$

Eq. (A8) underlines that the velocity of the free end of a specimen is proportional to the compression pulse striking the free end.

Appendix B. Exemplary illustration of the Novikov formula (35)

The Novikov formula is based on the assumptions that the stress is uniformly distributed in every cross-section of the specimen, and that the specimen is split *instantaneously* into two pieces, once the most strongly loaded cross-section is subjected to a tensile stress being equal to the *high-dynamic tensile strength* of the material. A specific example is used to highlight that the formula is valid for a non-symmetric bilinear stress pulse, characterized by an increase of the stress which is faster than the subsequent decrease, see Fig. B.1 (a).

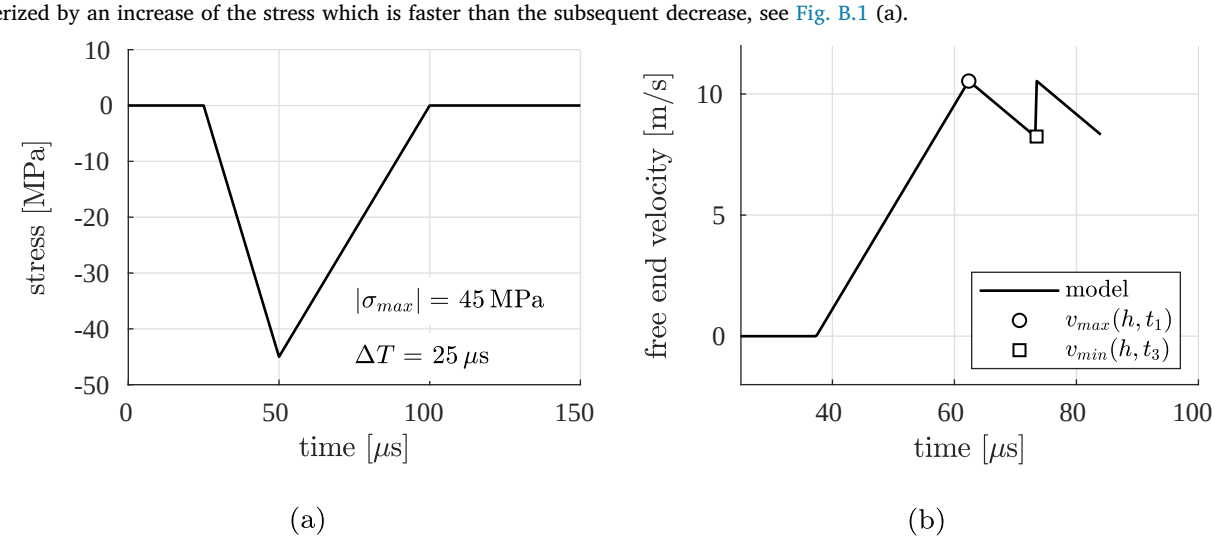

Fig. B.1. (a) Bilinear stress pulse; (b) velocity at the free end of the specimen.

A cylindrical specimen with properties equal to the specimens tested by Erzar and Forquin, see Table 1, is analyzed. The maximum amplitude of

the analyzed stress pulse amounts to 45 MPa. The increase of the stress from zero up to this maximum takes 25 μs. The subsequent decrease of the stress from the maximum back to zero takes 50 μs. The high-dynamic strength of the material is set equal to f_{dyn} = 10 MPa. The analysis is based on wave propagation in a linear-elastic, isotropic, homogeneous bar. It focuses on three time instants.

t_1 denotes the time instant of arrival of the maximum of the compression pulse at the free end of the specimen, see Fig. B.2(b). Thus, also the maximum of the reflected tension pulse is located at the free end, such that the stress-free boundary condition is satisfied. At time instant t_1, the effective stress is still compressive throughout the specimen, and the velocity of the free end of the specimen reaches its maximum, see Fig. B.1(b). For time instants $t > t_1$, tensile stresses will prevail at least in some parts of the specimen. The largest tensile stress will be located at the position of the maximum of the reflected tension pulse.

t_2 denotes the time instant at which the high-dynamic tensile strength is reached in the most strongly loaded cross-section. Its position is denoted as x_c, see Fig. B.2(c). There, the effective stress is tensile and its amplitude amounts to f_{dyn}. The amplitude of the incoming compression pulse amounts to $(-|\sigma_{max}| + f_{dyn})$ and that of the reflected tension pulse to $+\ |\sigma_{max}|$. It is assumed that the *entire* cross-section at the position x_c cracks instantaneously at the time instant t_2. The further analysis focuses on the part of the specimen between the cracked cross-section and the free end: $x \in [x_c; h]$. The tension pulse, striking the crack, is reflected. Thus, it is referred to as the "reflected tension pulse". It follows the tail of the incoming compression pulse, which passed the cross-section at position x_c right before the time instant t_2. The moving boundary between the tail of incoming compression pulse and the reflected tension pulse marks the position of a stress discontinuity, because the stress amplitude at the tail of the incoming compression pulse amounts to $(-|\sigma_{max}| + f_{dyn})$, see above, while the amplitude at the beginning of the twice reflected compression pulse is equal to $-|\sigma_{max}|$.

t_3 denotes the time instant of arrival of the described stress discontinuity at the free end of the specimen, see Fig. B2 (d). Up to the time instant t_3, the incoming compression pulse strikes the free end. The velocity at the free end of the specimen is proportional to the incoming compression pulse, see Fig. B.1(b). Once the stress discontinuity strikes the free end, the velocity jumps back to its maximum value, see Fig. B.1(b).

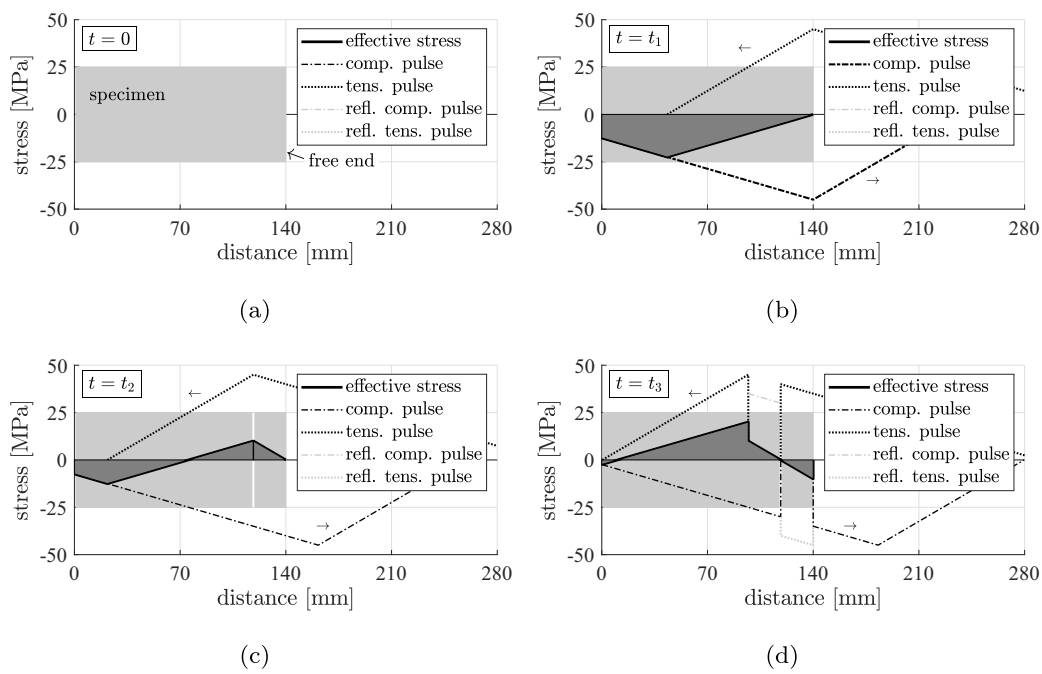

Fig. B.2. High-dynamic tension test: stresses along the axis of a specimen with a length of 140 mm, at different time instants: (a) before loading, (b) at the arrival of the maximum of the compression pulse at the free end, (c) when the high-dynamic tensile strength is reached in the most strongly loaded cross-section, (d) at the arrival of the stress discontinuity at the free end.

From the presented analysis, based on the assumptions that a specimen remains intact until the high-dynamic tensile strength of the material is reached in the most strongly loaded cross-section, and that this cross-section will fail instantaneously, the following conclusions are drawn:

- The *discontinuity* of the velocity of the free end of the specimen is proportional to f_{dyn}.
- The Novikov formula, stating that the difference between the maximum and the following minimum of the velocity of the free end of the specimen is proportional to f_{dyn}, is valid for a non-symmetric bilinear stress pulse, characterized by an increase of the stress which is faster than the subsequent decrease.
- For incoming compression pulses of arbitrary shape, the Novikov formula is an approximation.
- If the most strongly loaded cross-section would fail *instantaneously*, once the high-dynamic tensile strength is reached, the history of the velocity of the free end of the specimen would have to exhibit a *discontinuity*. Such a discontinuity was not observed in the measurements by Erzar and Forquin, see Fig. 14.
- The continuous model-predictions illustrated in Fig. 14 agree with the continuous measurements by Erzar and Forquin. The continuous nature of the model-predictions is related to *progressive* (rather than instantaneous) crack propagation, and *partial* (rather than total) reflection of pulses striking the cross-section that contains the crack.

Although the derivation of the Novikov formula remains, at least to a certain degree, unclear, the main result of the presented study is not affected. The proposed model is used to recalculate the quantities measured by Erzar and Forquin. The computed quantities are postprocessed by analogy to

the strategy used by Erzar and Forquin for the evaluation of their test data (including application of the Novikov formula). The results obtained from the model-based re-analysis are compared with the results of the experimental study. This way, it was shown that the underlying modeling idea agrees reaslonably well with the experimental observations of Erzar and Forquin.

References

[1] Y. Tai, Uniaxial compression tests at various loading rates for reactive powder concrete, Theor. Appl. Fract. Mech. 52 (1) (2009) 14–21.
[2] DIN EN, 12390-3:, Prüfung von Festbeton–Teil 3 [Testing of hardened concrete–Part 3]: Druckfestigkeit von Probekörpern [Compressive strength of specimens], Deutsche Fassung (2009).
[3] P. Bischoff, S. Perry, Compressive behaviour of concrete at high strain rates, Mater. Struct. 24 (6) (1991) 425–450.
[4] Z. Xu, H. Hao, H. Li, Experimental study of dynamic compressive properties of fibre reinforced concrete material with different fibres, Mater. Des. 33 (2012) 42–55.
[5] I. Fischer, B. Pichler, E. Lach, C. Terner, E. Barraud, F. Britz, Compressive strength of cement paste as a function of loading rate: experiments and engineering mechanics analysis, Cem. Concr. Res. 13 (58) (2014) 186–200.
[6] D.L. Grote, S.W. Park, M. Zhou, Dynamic behavior of concrete at high strain rates and pressure: I. Experimental characterization, Int. J. Impact Eng. 25 (9) (2001) 869–886.
[7] J.R. Klepaczko, A. Brara, An experimental method for dynamic tensile testing of concrete by spalling, Int. J. Impact Eng. 25 (14) (2001) 387–409.
[8] A. Brara, J.R. Klepaczko, Fracture energy of concrete at high loading rates in tension, Int. J. Impact Eng. 34 (14) (2007) 424–435.
[9] C.A. Ross, J.W. Tedesco, S.T. Kuennen, Effects of strain rate on concrete strength, Materials Journal 92 (1) (1995) 37–47.
[10] G. Gary, P. Bailly, Behaviour of quasi-brittle material at high strain rate. Experiment and modelling, Eur. J. Mech. A. Solids 17 (3) (1998) 403–420.
[11] B. Riisgaard, T. Ngo, P. Mendis, C. Georgakis, H. Stang, Dynamic increase factors for high performance concrete in compression using split Hopkinson pressure bar, Proceedings of 6th International Conference on Fracture Mechanics of Concrete and Concrete Structures, 3 2007, pp. 1467–1471.
[12] M. Zhang, H. Wu, Q. Li, F. Huang, Further investigation on the dynamic compressive strength enhancement of concrete-like materials based on split Hopkinson pressure bar tests. Part I: Experiments, Int. J. Impact Eng. 36 (12) (2009) 1327–1334.
[13] B. Erzar, P. Forquin, Experiments and mesoscopic modelling of dynamic testing of concrete, Mech. Mater. 46 (14) (2011) 505–527.
[14] B. Erzar, P. Forquin, Analysis and modelling of the cohesion strength of concrete at high strain rates, Int. J. Solids Struct. 51 (14) (2014) 2559–2574.
[15] T. Kühn, C. Steinke, Z. Sile, I. Zreid, M. Kaliske, M. Curbach, DynamischeEigenschaften von Beton im Experiment und in der Simulation [Dynamic properties of concrete in experiment and simulation], Beton- und Stahlbeton 111 (1) (2016) 41–50.
[16] D. Lu, G. Wang, X. Du, Y. Wang, A nonlinear dynamic uniaxial strength criterion that considers the ultimate dynamic strength of concrete, Int. J. Impact Eng. 103 (2017) 124–137.
[17] fib Model Code for Concrete Structures 2010, Ernst & Sohn, 2010.
[18] J. Tedesco, C. Ross, Strain-rate-dependent constitutive equations for concrete, J. Pressure Vessel Technol. 120 (4) (1998) 398–405.
[19] Q. Li, H. Meng, About the dynamic strength enhancement of concrete-like materials in a split Hopkinson pressure bar test, Solids and Structures 40 (2003) 343–360.
[20] X. Zhou, H. Hao, Modelling of compressive behaviour of concrete-like materials at high strain rate, Int. J. Solids Struct. 45 (17) (2008) 4648–4661.
[21] Y. Hao, H. Hao, Z. Li, Influence of end friction confinement on impact tests of concrete material at high strain rate, Int. J. Solids Struct. 60 (2013) 82–106.
[22] Y. Al-Salloum, T. Almusallam, S. Ibrahim, H. Abbas, S. Alsayed, Rate dependent behavior and modeling of concrete based on SHPB experiments, Cem. Concr. Compos. 55 (2015) 34–44.
[23] S. Hentz, F.V. Donzé, L. Daudeville, Discrete element modelling of concrete submitted to dynamic loading at high strain rates, Comput. Struct. 82 (29-30) (2004) 2509–2524.
[24] D. Cotsovos, M. Pavlovic, Numerical investigation of concrete subjected to compressive impact loading. Part 1: A fundamental explanation for the apparent strength gain at high loading rates, Comput. Struct. 86 (2008) 145–163.
[25] E. Flores-Johnson, Q. Li, Structural effects on compressive strength enhancement of concrete-like materials in a split Hopkinson pressure bar test, Int. J. Impact Eng. 109 (2017) 408–418.
[26] H. Mihashi, F. Wittmann, Stochastic approach to study the influence of rate of loading on strength of concrete, Heron 25 (1980) 54.
[27] Z. Bažant, F. Caner, M. Adley, S. Akers, Fracturing rate effect and creep in microplane model for dynamics, J. Eng. Mech. 126 (2000) 962–970.
[28] J. Georgin, J. Reynouard, Modeling of structures subjected to impact: concrete behaviour under high strain rate, Cem. Concr. Compos. 25 (1) (2003) 131–143.
[29] X. Wang, Z. Yang, J. Yates, A. Jivkov, C. Zhang, Monte Carlo simulations of mesoscale fracture modelling of concrete with random aggregates and pores, Construct. Build Mater. 75 (2015) 35–45.
[30] P. Otto, L. De Lorenzis, J.F. Unger, A regularized model for impact in explicit dynamics applied to the split Hopkinson pressure bar, Comput. Mech. 58 (4) (2016) 681–695.
[31] J. Ožbolt, A. Sharma, H.-W. Reinhardt, Dynamic fracture of concrete–compact tension specimen, Int. J. Solids Struct. 48 (10) (2011) 1534–1543.
[32] Y. Hao, H. Hao, X. Zhang, Numerical analysis of concrete material properties at high strain rate under direct tension, Int. J. Impact Eng. 39 (1) (2012) 51–62.
[33] F. Gatuingt, G. Pijaudier-Cabot, Coupled damage and plasticity modelling in transient dynamic analysis of concrete, Int. J. Numer. Anal. Methods Geomech. 26 (1) (2002) 1–24.
[34] L. Snozzi, A. Caballero, J.-F. Molinari, Influence of the meso-structure in dynamic fracture simulation of concrete under tensile loading, Cem. Concr. Res. 41 (11) (2011) 1130–1142.
[35] O. Yılmaz, J.-F. Molinari, A mesoscale fracture model for concrete, Cem. Concr. Res. 97 (2017) 84–94.
[36] H. Kolsky, An investigation of the mechanical properties of martials at very high rates of loading, Proc. Phys. Soc. 43 (14) (1949) 505–527.
[37] L. Freund, Crack propagation in an elastic solid subjected to general loading – I. Constant rate of extension, J. Mech. Phys. Solids 20 (3) (1972) 129–140.
[38] E.E. Abraham, H. Gao, How fast can cracks propagate? Phys. Rev. Lett. 84 (14) (2007) 3113–3116.
[39] A.J. Watson, W.F. Anderson, B. Archer, Hypervelocity impact of concrete, Proceeding of the RILEM-CEB-IABSE-IASS Symposium on Concrete Structures under Impact and Impulsive Loading, Berlin, 1982, pp. 188–201.
[40] M. Curbach, J. Eibl, Crack velocity in concrete, Eng. Fract. Mech. 35 (1-3) (1990) 321–326.
[41] E. Binder, H. Wang, T. Schlappal, J. Zhang, Y. Yuan, B. Pichler, H. Mang, Bridging the gap between concrete microstructures and tunnel linings, Advances in Computational Plasticity, Springer, 2018, pp. 23–44.
[42] A. Brara, Étude expérimentale de la traction dynamique du béton par écaillage [Experimental study of dynamic tension of concrete via spalling], Ph.D. thesis Metz University France, in French, 1999.
[43] A. Brara, F. Camborde, J. Klepaczko, C. Mariotti, Experimental and numerical study of concrete at high strain rates in tension, Mech. Mater. 33 (1) (2001) 33–45.
[44] S. Novikov, I. Divnov, A. Ivanov, Failure of steel, aluminium and copper under explosive shock loading, Phys. Met. Metallogr. 21 (4) (1966) 122–128.
[45] S. Sharma, V. Chavan, R. Agrawal, R. Patel, R. Kapoor, J. Chakravartty, Split-Hopkinson Pressure Bar: An Experimental Technique for High Strain Rate Tests, Tech. rep. Bhabha Atomic Research Centre, 2011.
[46] W. Drugan, J. Willis, A micromechanics-based nonlocal constitutive equation and estimates of representative volume element size for elastic composites, J. Mech. Phys. Solids 44 (4) (1996) 497–524.
[47] M. Königsberger, B. Pichler, C. Hellmich, Micromechanics of ITZ-aggregate interaction in concrete part I: Stress concentration, J. Am. Ceram. Soc. 97 (2) (2013) 535–542.
[48] M. Königsberger, B. Pichler, C. Hellmich, Micromechanics of ITZ-aggregate interaction in concrete part II: strength upscale, J. Am. Ceram. Soc. 97 (2) (2014) 5516–5543.
[49] K.L. Scrivener, A.K. Crumbie, P. Laugesen, The interfacial transition zone (ITZ) between cement paste and aggregate in concrete, Interface Sci. 12 (4) (2004) 411–421.
[50] Z. Bažant, Y. Xi, Statistical size effect in quasi-brittle structures: II. Nonlocal theory, J. Eng. Mech. 117 (11) (1991) 2623–2640.
[51] H. Schuler, Experimentelle und numerische Untersuchungen zur Schädigung von stoßbeanspruchtem Beton [Experimental and numerical damage analysis of shock-loaded concrete], Ph.D. thesis Fraunhofer Institut für Kurzzeitdynamik, 2004.
[52] P. Acker, F.-J. Ulm, Creep and shrinkage of concrete: physical origins and practical measurements, Nucl. Eng. Des. 203 (2-3) (2001) 143–158.
[53] S. Widehammar, A Method for Dispersive Split Hopkinson Pressure Bar Analysis Applied to High Strain Rate Testing of Spruce Wood, Uppsala University, 2002 Ph.D. thesis.
[54] W.J. Stronge, Wave Propagation from Impact on Slender Deformable Bodies, 2nd Edition, Cambridge University Press, 2018, pp. 148–176.